# Comparative Study of Analytical and Machine Learning Models for Gamma Source Localization in Waste Drums

**Authors:** Lee, Sangjun, Kim, Seunghyeon, Park, Mr. Jae Hyung, Kim, Mr. Jinhong, Cho, Prof. Seung Hyun, Huh, Prof. Chulhaeng, Lee, Prof. Bongsoo, Lee, Prof. Bongsoo

**Date:** 2025-11-08T17:45:23+00:00

## Abstract

In this study, we compared analytical and machine learning models for two-dimensional nondestructive localization of radioactive sources within a simulated waste drum. A 60Co gamma source was located at 72 different positions within the simulated drum. A reflector-coated liquid light guide (LLG) system detected the Cherenkov radiation generated by 60Co source. Time-of-flight measurements revealed that time differences of the source peaks correlated linearly with angular position, while their amplitudes exhibited complex dependencies on both radial and angular coordinates. For 24 arbitrary source positions, an analytical localization model achieved mean absolute errors of 2.024 cm for radial distance and 5.940° for angular position, with an overall Euclidean error of 2.518 cm. However, model performance degraded significantly at the LLG intersection region and at small radial distances where signal intensity decreased. To address these limitations, a multilayer perceptron (MLP) neural network was developed and reduced errors to 0.601 cm radially, 4.703° angularly, and 1.181 cm in Euclidean distance. The use of the MLP neural network represents improvements of 70.31%, 20.82%, and 53.10%, respectively. The neural network model successfully resolved localization challenges in geometrically complex regions by capturing nonlinear spectral-spatial relationships. These findings demonstrate that integrating machine learning with localization enhances radioactive waste characterization capabilities.

## Full Text

## Preamble

### Comparative Study of Analytical and Machine Learning Models for Gamma Source Localization in Waste Drums

Sangjun Leea, Seunghyeon Kima, Jae Hyung Parka, Jinhong Kima, Seung Hyun Chob, Chulhaeng Huhc, and Bongsoo Leea*

a School of Energy Systems Engineering, Chung-Ang University, Seoul, 06974, South Korea
b Department of Materials Science and Engineering, Soong-sil University, Seoul, 06978, South Korea
c Department of Radiation Oncology, Augusta University, Georgia, 30912, USA

*Corresponding author. Email: bslee@cau.ac.kr

## Abstract

In this study, we compared analytical and machine learning models for two-dimensional nondestructive localization of radioactive sources within a simulated waste drum. A 60Co gamma source was located at 72 different positions within the simulated drum. A reflector-coated liquid light guide (LLG) system detected the Cherenkov radiation generated by the 60Co source. Time-of-flight measurements revealed that time differences of the source peaks correlated linearly with angular position, while their amplitudes exhibited complex dependencies on both radial and angular coordinates. For 24 arbitrary source positions, an analytical localization model achieved mean absolute errors of 2.024 cm for radial distance and 5.940° for angular position, with an overall Euclidean error of 2.518 cm. However, model performance degraded significantly at the LLG intersection region and at small radial distances where signal intensity decreased. To address these limitations, a multilayer perceptron (MLP) neural network was developed and reduced errors to 0.601 cm radially, 4.703° angularly, and 1.181 cm in Euclidean distance. The use of the MLP neural network represents improvements of 70.31%, 20.82%, and 53.10%, respectively. The neural network model successfully resolved localization challenges in geometrically complex regions by capturing nonlinear spectral-spatial relationships. These findings demonstrate that integrating machine learning with localization enhances radioactive waste characterization capabilities.

**Keywords:** Liquid light guide, Time-of-flight, Position-sensitive, Cherenkov radiation, Reflector

## 1. Introduction

The safe management and continuous monitoring of radioactive waste remain critical challenges in the context of long-term storage and environmental protection. Radioactive waste generated from nuclear power plants poses complex radiological risks during handling, transportation, and storage. To mitigate these risks, radioactive waste packaging must maintain structural integrity, containment, and confinement capabilities throughout interim storage or permanent disposal to provide adequate protection against radiological hazards [1-3]. Among the radionuclides present in radioactive waste, 60Co represents a particularly significant isotope due to its distinctive gamma ray energies [4]. 60Co emits gamma rays with energies of 1.173 and 1.332 MeV, and these high-energy gamma rays make 60Co a significant contributor to external dose rates and shielding requirements during storage. These characteristic gamma ray energies enable reliable detection, thereby classifying 60Co as an easy-to-measure (ETM) nuclide. The scaling factor (SF) method employs ETM nuclide measurements as primary indicators for estimating difficult-to-measure (DTM) nuclide activities. The SF method has become a standard methodology for characterizing radionuclide inventories in radioactive waste, particularly for DTM nuclides that cannot be readily quantified through direct measurement. This approach exploits the correlation between ETM and DTM nuclides to derive quantitative estimates of DTM nuclide activities [5]. Precise determination of information on ETM nuclides remains essential for implementation of the SF method.

Disposal facilities require monitoring infrastructure to ensure safe containment of radioactive materials and enable detection of potential releases through continuous surveillance of storage conditions. Nondestructive assay (NDA) has emerged as the internationally recognized standard for achieving the necessary measurement precision [6]. NDA techniques play a significant role in the classification and verification of radioactive waste without requiring invasive sampling that could compromise containment integrity. The American Society for Testing and Materials (ASTM) International recognizes segmented gamma scanning (SGS) and tomographic gamma scanning (TGS) as standard NDA techniques [7-9]. Los Alamos National Laboratory (LANL) constructed the first commercial SGS and TGS systems. However, these standard NDA techniques have certain limitations. SGS assumes homogeneous distribution of both matrix material and radioactive content throughout the waste drum; deviations from this assumption can produce assay errors exceeding 100% [10]. LANL addressed this limitation by developing the TGS method, and TGS substantially improves measurement accuracy. However, it requires a more complex detection process and longer measurement times than SGS [11-12].

Researchers have explored promising solutions using time-of-flight (ToF)-based detection systems to address these challenges [13-15]. ToF methods localize source positions by measuring the time differences of radiation-induced signals arriving at one or more detectors. These techniques enable cost-effective monitoring over large areas when combined with optical fibers.

An effective tool for ToF detectors is a plastic scintillating fiber (PSF). PSFs serve a dual function: detecting radiation and transmitting the resulting light. They maintain the core-cladding structure of conventional optical fibers but incorporate fluorescent agents within the core material. When radiation interacts with the core material of PSF, scintillation light is generated and transmitted to both ends through its axis. This combination of radiation detection via scintillation and efficient optical transmission makes PSFs well-suited for radiation monitoring applications [16-18].

Researchers have investigated the use of Cherenkov radiation in parallel with scintillation-based systems. Cherenkov radiation is typically considered an unwanted background signal in scintillation detectors due to its lower intensity compared to scintillation [19-21]. However, Cherenkov radiation offers distinct advantages that differentiate it from scintillation: fast response times, directional emission, and a characteristic emission spectrum spanning the UV-visible wavelength range [22].

Plastic, quartz, and glass optical fibers have demonstrated effectiveness as Cherenkov radiation sensors due to their optical transparency and high transmittance properties [23-25]. However, the inherently lower light yield of Cherenkov radiation necessitates the use of fiber bundles to achieve adequate signal levels. The dead zones between fibers in traditional fiber bundles can result in incomplete photon capture and compromise light collection efficiency. To address these limitations, liquid light guides (LLGs) have been developed, which can increase the effective detection area without introducing inter-fiber dead zones.

Numerous studies have investigated the characteristics of LLGs and demonstrated their feasibility for radionuclide localization through ToF methods utilizing Cherenkov radiation [26-29]. LLGs consist of a liquid-filled core enclosed within a polymer tube and feature substantially larger diameters than conventional optical fibers. This increased diameter extends the interaction path length for charged particles, thereby enhancing Cherenkov radiation generation. Each end of an LLG incorporates a fused-silica window with an open-pipe configuration, which eliminates the dead zones inherent in fiber bundles and maximizes light collection efficiency. Additionally, LLGs demonstrate distinct advantages over conventional optical fibers: low attenuation coefficients and superior transmittance across the UV-Vis wavelength range. Due to these properties, LLGs are suitable for radiation detection applications.

Our recent studies have demonstrated the effectiveness of reflector-coated LLGs in source localization. By coating an LLG with a reflector at one end and coupling a photomultiplier tube (PMT) at the opposite end, accurate one-dimensional localization has been achieved [30]. However, challenges remain when the radiation source is located away from the LLG. In such scenarios, the Cherenkov intensity diminishes because fewer gamma rays reach the LLG due to the inverse square law, resulting in fewer Compton scattering interactions and consequently fewer Cherenkov photons being generated. Conventional analytical models that rely on curve fitting methods and are based on geometrical assumptions often struggle to interpret low-intensity signals accurately under these conditions. This has led to the adoption of machine learning (ML)-based approaches, which are well-suited to handling nonlinear data. Neural network models can localize source positions more accurately than conventional methods, particularly in challenging measurement conditions [14,31].

In this study, we compared analytical and ML-based models for two-dimensional nondestructive localization of a gamma-emitting source inside a simulated radioactive waste drum. A 60Co disk-type source was located at various positions inside a drum to emulate realistic waste geometries, and the LLG was wound once around the circumference of a simulated drum. At each source position, Cherenkov light was collected via a reflector-coated LLG system using ToF measurements. The collected Cherenkov light generates the position spectra, and these spectra were analyzed as a function of source position using cylindrical coordinates. These spectral variations formed the basis for developing an analytical localization model. To assess the potential enhancement from ML techniques, a multilayer perceptron (MLP) neural network was trained on the same position spectral data. Both models were validated using the training dataset and subsequently tested on arbitrary source positions not included in the training data. The performance of the analytical localization model was compared with an ML-based approach using MLP neural networks. The performances of both models were evaluated using mean absolute errors (MAEs) in radial distance, angular position, and Euclidean distance.

## 2.1. Cherenkov radiation

When a charged particle travels through a medium at a speed exceeding the speed of light in that medium, the medium becomes polarized by the charged particle, and the polarized medium emits coherent, directional radiation [32]. This phenomenon is known as Cherenkov radiation and was first characterized by Pavel Cherenkov in 1934. Cherenkov radiation has become a fundamental detection principle due to its unique threshold behavior and directional emission characteristics. The charged particle must possess sufficient kinetic energy exceeding a specific threshold value to emit Cherenkov radiation, which is called the Cherenkov threshold energy (CTE). In a medium with a constant refractive index of n, the CTE of electrons, denoted by $E_{th}^{e}$, can be calculated using the following relation:

$$E_{th}^{e} = m_{ec}^{2}\left(\frac{n}{\sqrt{n^2-1}} - 1\right)$$

where $m_{ec}^{2}$ is the electron rest-mass energy (0.511 MeV) [23]. For the core materials of typical optical fibers whose refractive indices range from 1.4 to 1.6, the calculated CTEs of electrons are approximately 0.219 MeV and 0.144 MeV, respectively. These threshold energies determine whether secondary electrons produced by gamma ray interactions can generate Cherenkov radiation.

While electrically neutral gamma rays cannot produce Cherenkov radiation directly due to their lack of electric charge, charged particles such as alpha and beta particles can directly generate Cherenkov radiation. However, when gamma rays interact with medium, various mechanisms can produce secondary charged particles. The type of interaction and the resulting energy distribution of secondary particles are governed by both the energy of the incident gamma ray and the atomic number of the target material. In the case of an LLG that is predominantly composed of low-atomic-number elements, Compton scattering is the dominant interaction mechanism for incident gamma rays. During Compton scattering, the incident gamma ray transfers a portion of its energy to an orbital electron, ejecting it from the atom. This ejected electron is called a Compton electron.

When the gamma ray is incident on the optical fiber, Cherenkov radiation is emitted if the kinetic energy of the resulting Compton electron exceeds the CTE of electrons in the medium. The Compton electron achieves maximum energy when the gamma ray is scattered at 180°. The maximum energy of a Compton electron produced by a gamma ray of energy $E_\gamma$ can be calculated using the following equation [32]:

$$E_{e,max} = \frac{E_\gamma}{1 + \frac{m_{ec}^2}{2E_\gamma}}$$

The energy of incident gamma ray is a crucial factor in determining whether Compton electrons can exceed the Cherenkov threshold. The CTE of gamma rays $E_{th}^{\gamma}$, the minimum gamma ray energy required to produce Cherenkov radiation, can be derived by combining Eq. 1 and Eq. 2:

$$E_{th}^{\gamma} = \frac{m_{ec}^2}{2}\left(\frac{n}{\sqrt{n^2 - 1}} - 1\right)$$

For 60Co, gamma rays with energies of 1.173 MeV and 1.332 MeV generate Compton electrons with maximum energies of 0.963 MeV and 1.118 MeV, respectively. These energies exceed the CTE of electrons for typical optical fibers, as shown in Fig. 1 [FIGURE:1].

**Fig. 1.** Cherenkov threshold energies of electrons and gamma rays as a function of refractive index.

## 2.2. Experimental setup

**Fig. 2** [FIGURE:2]. Experimental setup for two-dimensional localization of a 60Co source using a reflector-coated LLG system.

Fig. 2 illustrates the experimental setup employing a reflector-coated LLG for Cherenkov light detection. One end of an LLG (Series 300, 5 mm diameter, 5 m length, Lumatec) was coated with a reflector (PF03-03-F01, Thorlabs), while the opposite end was optically coupled to a PMT module (H10721P-01, Hamamatsu Photonics) via a silicone-rubber-based optical interface (EJ-560, Eljen

Technology) for refractive index matching. Blackout fabric (BK5, Thorlabs) was used to cover both ends of the LLG to eliminate ambient light interference. The PMT module converted the incoming light into electrical signals, which were amplified by a fast amplifier (ABL0300-00-4030, WENTEQ) and subsequently recorded with an oscilloscope (SDS5104X, Siglent). The oscilloscope operated at a constant sampling rate of 5 GS/s to acquire signals with high temporal precision. Detailed specifications of the oscilloscope and PMT module are provided in Tables 1 and 2, respectively.

**Table 1** . Specifications of SDS-5104X

| Properties | Value |
|---|---|
| Sample rate [GS/s] | 5 |
| Bandwidth [GHz] | 1 |
| Vertical resolution [bit] | 10 |
| Maximum waveform capture rate [wfm/s] | 500,000 |
| Minimum time limit for trigger [ns] | 8 |
| Trigger resolution [ns] | 1 |

**Table 2** . Specific properties of H10721P-01

| Properties | Value |
|---|---|
| Spectral response [nm] | 230 ~ 870 |
| Peak sensitivity wavelength [nm] | 400 |
| Effective area [mmΦ] | 8 × 8 |
| Typical dark current [s-1] | 50 |
| Rise time [ns] | 0.57 |

To localize the radioactive sources within the simulated waste drum, the LLG was wound once around the circumference of a cylindrical drum with a radius of 21 cm. This configuration created an intersection region where the LLG crosses itself. In this region, gamma rays can generate Cherenkov radiation in both LLG segments, producing signals for two positions simultaneously.

Since the LLG intersects itself at the point where the LLG starts and completes its circular path, signals detected from both segments correspond to angular positions of 0° and 360°. In this experimental setup, they represent the same physical position but appear as distinct peaks in the position spectrum. This phenomenon presents a challenge for conventional analytical models, as discussed in Section 3.

The intensity of Cherenkov radiation plays a critical role in its detection. The number of Cherenkov photons per unit path length and per unit path wavelength, denoted as $\frac{d^2N}{dld\lambda}$, can be expressed by the following relation:

$$\frac{d^{2N}}{dld\lambda} = \frac{2\pi\alpha z^2}{\lambda^2}\left(1-\frac{1}{\beta^{2n^2}}\right)$$

where $\alpha$ is the fine structure constant (1/137), z is the electric charge of the particle in units of elementary charge (z = 1 for electrons), and $\beta$ is the ratio of the particle velocity to the speed of light in a vacuum [33]. As shown in Eq. 4, the intensity of Cherenkov radiation exhibits wavelength dependence. Specifically, the number of photons is proportional to $1/\lambda^2$. This proportionality means that higher photon yields occur at shorter wavelengths, resulting in significantly enhanced emission in the UV-visible region compared to longer wavelengths. Consequently, the performance of the optical sensing system is highly sensitive to the spectral response characteristics of its constituent components, including the LLG, PMT, and reflector. These components must exhibit high transmittance or reflectance across the UV-Vis wavelength range to ensure efficient photon collection and detection.

**Fig. 3**

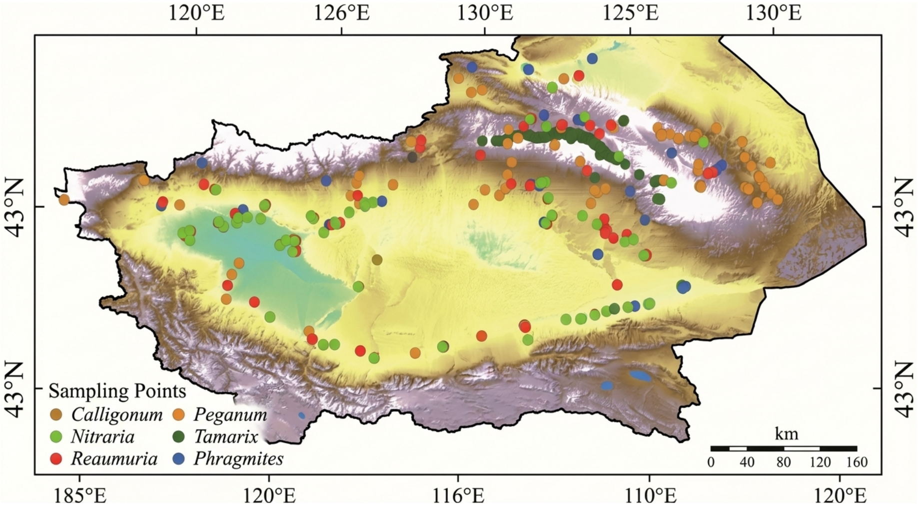

Figure 1: Figure 3

. Spectral characteristics of the LLG, reflector, and PMT module in the UV-Vis wavelength range.

Fig. 3 presents the spectral characteristics of the optical detection system, including the transmittance of the LLG, the reflectance of the reflector, and the quantum efficiency of the PMT module. The LLG, which serves as both a Cherenkov light generation medium and a light guide, demonstrates excellent optical transmittance in the 250-750 nm wavelength range [34]. The reflector exhibits a reflectance greater than 90% in the 250-450 nm wavelength range

[35]. The PMT module can detect light across a broad spectral range of 250-850 nm and exhibits peak quantum efficiency at approximately 400 nm, making it well-suited for maximizing Cherenkov light collection [36].

## 2.3. Time-of-Flight method

When Cherenkov radiation is generated within the LLG core, the Cherenkov photons propagate bidirectionally along the LLG via total internal reflection (TIR). TIR is a fundamental optical principle in which light traveling from a medium with a higher refractive index to one with a lower refractive index is completely reflected at the interface. This occurs when the incident angle of the light exceeds the critical angle at the interface. In the case of Cherenkov radiation, the characteristic angle of Cherenkov photon emission, known as the Cherenkov angle, and the critical angle of the LLG are crucial parameters for TIR. The Cherenkov angle, denoted as $\theta_c$, is determined by the kinetic energy of the Compton electron $E_e$, as shown in Eq. 5:

$$\theta_c = \arccos\left(\frac{1}{\beta n}\right) = \arccos\left(\frac{E_e + m_{ec}^2}{n\sqrt{E_e(E_e + 2m_{ec}^2) + (m_{ec}^2)^2}}\right)$$

For photons to propagate along the LLG, the emission angle of the Cherenkov photons, determined by both the Compton electron trajectory and the Cherenkov angle, must satisfy the TIR condition at the core-cladding interface. The critical angle depends on the refractive indices of both the core and cladding materials, but the specific refractive indices of the LLG components were not provided by the manufacturer.

The source position within the drum is determined from the time difference between two signals detected by the PMT module. The photons reach the PMT module either directly or after reflection from the far-end reflector. The time difference between the Cherenkov photons arriving at the PMT module depends on the path-length difference, as shown in Fig. 4 [FIGURE:4].

**Fig. 4.** ToF-based localization through total internal reflection using reflector-coated LLG.

If the Cherenkov radiation is generated by a radioactive source at position x along an LLG of length L, photons traveling directly to the PMT traverse a distance x, while those reflected from the far-end reflector traverse a distance 2L−x. Consequently, the time difference between the two signals, denoted as T, can be expressed as a function of x and L:

$$T = \frac{2(L - x)}{v_g}$$

where $v_g$ is the group velocity of light in the LLG.

## 2.4. Data acquisition

When a signal enters the oscilloscope and its amplitude exceeds the amplitude threshold, it is recorded by leading-edge timing. When two signals meet the leading-edge threshold within a defined time window, the oscilloscope captures both signals simultaneously using interval triggering. However, the inherent limitation of leading-edge timing is its susceptibility to amplitude walk. Variations in signal amplitudes affect the time at which the signal crosses the amplitude threshold. Furthermore, discrepancies in rise time between the two signals can introduce additional timing errors. These effects reduce the accuracy of time-difference measurements, thereby compromising localization accuracy. To address these limitations, Amplitude and Rise-time Compensation (ARC) triggering was employed.

ARC triggering is a commonly used crossover-timing method that converts signals into bipolar waveforms to improve timing precision. The use of ARC triggering offers immunity to amplitude fluctuations and improves the precision of time-difference measurements regardless of variations in signal rise time [37]. The raw signal is attenuated through multiplication by a constant k (where $-1 < k < 0$). The attenuated signal is delayed by a fixed time interval and then summed with the raw signal. This delay time is chosen to be less than the rise time of the raw signal to ensure that the resulting signal crosses zero before reaching its maximum amplitude. Both signals captured simultaneously by the oscilloscope were converted into bipolar waveforms through ARC triggering, and the time difference between the zero crossings of the two waveforms was measured.

The implementation of ARC triggering is illustrated in Fig. 5 [FIGURE:5].

**Fig. 5.** Amplitude and Rise-time Compensation triggering for precise time-difference measurements.

For two-dimensional source localization using cylindrical coordinates, measurement points were arranged at regular intervals in both radial distance and angular position. An uncollimated 60Co disk-type source with an activity of 23.451 Ci was positioned at 72 measurement points: radial distances from 1 cm to 21 cm in 4 cm increments, covering the full 360° angular range in 30° intervals. When the source is located at the center and inner wall of the drum, the radial distance is set to 0 cm and 21 cm, respectively. In other words, radial distance refers to the distance between the source and the center of the drum. In the intersection region, the angular position represents 0° and 360°. The angular position increases in the counterclockwise direction.

At each position, 10,000 paired signals with corresponding time differences were acquired. These signals constituted the training dataset, which was used both to derive the analytical localization model through curve fitting and to train the ML model through an MLP neural network. An additional 5,000 paired signals were collected from 24 arbitrary positions to evaluate the localization accuracy. Model performance was evaluated using the mean absolute error in radial distance, angular position, and Euclidean distance between the estimated and actual source positions.

## 3.1. Time difference

The spectral characteristics of position spectra dependent on source position provide the foundation for spatial localization methods. Position spectra were acquired using 10,000 paired signals obtained from 72 source positions and their bin width was set to 0.5 ns. The position spectra for different radial distances and angular positions were compared to investigate the influence of source position on spectral characteristics. For consistency, each position spectrum was normalized to a total count of 100.

**Fig. 6** [FIGURE:6]. Position spectra at various angular positions along the LLG at a radial distance of 21 cm.

Fig. 6 illustrates the position spectra at various angular positions along the LLG at a radial distance of 21 cm. Each spectrum consistently exhibits three distinct peaks. The peak that varies with angular position is defined as a source peak, indicating the actual source position. As shown in Fig. 6, the time difference of the source peak clearly shifts with changes in angular position. At a fixed radial distance, the amplitude of the source peak is greatest at the angular position of 180°, which is directly opposite the intersection region, and decreases as the angular position deviates from 180°. In particular, it decreases abruptly as the source approaches the intersection region. In the intersection region, the normalization process distributes the total counts between the two angular positions of 0° and 360°, resulting in characteristic dual low-intensity peaks. Nevertheless, the source peaks, including these dual low-intensity peaks, demonstrate high temporal stability with a maximum standard deviation of 0.336 ns or less across five repeated experiments. Table 3 summarizes the time differences of the source peak and their standard deviations.

**Table 3.** Time differences and standard deviations according to the source position

| Source position [degrees] | Time difference [ns] | StDev [ns] |
|---|---|---|
| 0 | 49.5 | 0.336 |
| 30 | 45.2 | 0.298 |
| 60 | 41.8 | 0.287 |
| 90 | 38.1 | 0.265 |
| 120 | 34.7 | 0.274 |
| 150 | 31.4 | 0.281 |
| 180 | 27.9 | 0.259 |
| 210 | 31.3 | 0.272 |
| 240 | 34.6 | 0.268 |
| 270 | 38.2 | 0.261 |

| Source position [degrees] | Time difference [ns] | StDev [ns] |
|---|---|---|
| 300 | 41.9 | 0.285 |
| 330 | 45.3 | 0.291 |

The two peaks appearing consistently at both ends of the spectra are referred to as reflection peaks. These reflection peaks arise from reflections at the LLG ends, which have been analyzed in prior studies [25-27]. In contrast to the angular-dependent characteristics of the source peak, the amplitudes of reflection peaks vary across all spectra but show no significant angular dependence.

**Fig. 7**

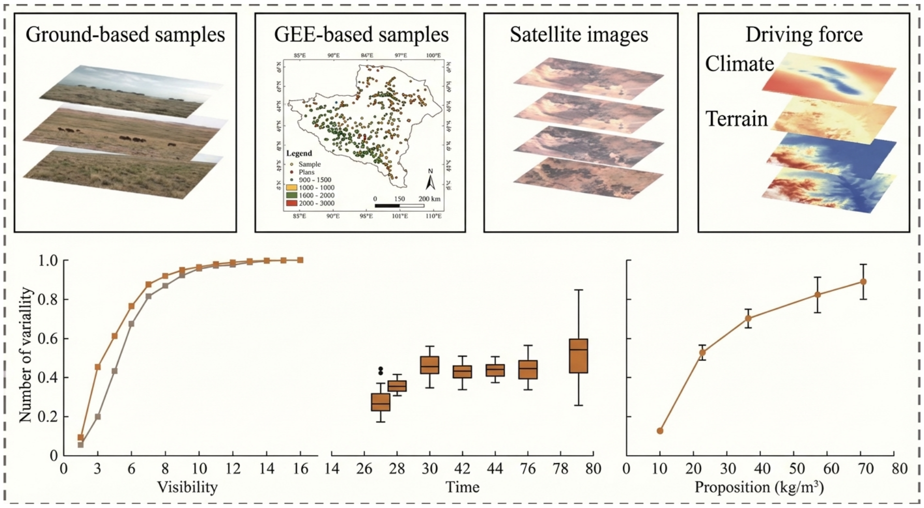

Figure 2: Figure 7

. Position spectra as a function of radial distance at a fixed angular position of 180°.

The influence of radial distance on spectral characteristics was also examined. Fig. 7 shows the position spectra at various radial distances for a fixed angular position of 180°. As shown in Fig. 7, the time difference of the source peak remained unchanged although radial distance varied. This invariance of time difference with radial distance indicates that the time difference of the source peak depends solely on angular position. In contrast, the amplitude of the source peak decreased and its width broadened with decreasing radial distance. As the radial distance decreases, the source moves farther from the LLG, causing gamma rays to spread over a wider area. This wider distribution increases the range of time differences, thereby leading to peak broadening. This peak broadening hinders accurate source localization, particularly near the intersection region and near the center of the drum. However, the reflection peaks showed no radial dependence, similar to their angular independence, maintaining consistent time differences, peak widths, and amplitudes across all spectra.

**Fig. 8** [FIGURE:8]. Comparison of position spectra for sources positioned at radial distances of 1 cm and 5 cm at angular positions of 90° and 270°.

Fig. 8 further illustrates the influence of peak broadening effects by comparing four position spectra: radial distances of 1 cm and 5 cm, each at angular positions of 90° and 270°. The position spectra at 1 cm (diamond markers) closely match those at 5 cm (solid lines), showing minimal variation despite the difference in radial distance. This similarity between spectra at different radial distances poses challenges in distinguishing the actual radial distance of the source position. This limitation reduces localization accuracy at small radial distances where peak broadening obscures radial distance information.

**Fig. 9** [FIGURE:9]. Variation of source peak amplitude with respect to source position in Cartesian coordinates.

Fig. 9 shows the variation of source peak amplitudes with respect to source position in Cartesian coordinates. As shown in Fig. 9, the amplitude of the source peak is high when the source is located at r = 21 cm and decreases progressively as the radial distance approaches r = 0 cm. Additionally, the intersection region, at x = 21 cm and y = 0 cm and corresponding to r = 21 cm at angular positions of 0° and 360°, exhibits markedly reduced amplitude despite the relatively high source peak amplitudes observed at other r = 21 cm positions. Despite these limitations observed at small radial distances and near the intersection region, the spectral dependence of source peak on the radial distance and angular position provides sufficient information for constructing a localization model based on spectral characteristics.

## 3.2. Analytical localization model

Quantifying the relationship between the source position and spectral dependence of source peak is essential for model construction. To construct an analytical localization model, the source position must be expressed as a function of the time difference and amplitude of the source peak, which exhibit different dependencies on source coordinates. As a result, the time difference and amplitude of the source peak also must be expressed as functions of the angular position and radial distance. As demonstrated in Figs. 6 and 7, the time difference of the source peak depends solely on angular position, remaining invariant with radial distance. Fig. 10 [FIGURE:10] illustrates this relationship, showing that the time difference varies linearly with angular position.

**Fig. 10.** Relationship between time differences of the source peak and angular position.

While the time difference characteristics enable angular localization, the amplitude characteristics are essential for radial distance determination. The amplitude of the source peak varies with changes in both radial distance and angular position. As shown in Fig. 9, the amplitude depends strongly on radial distance and exhibits weaker dependence on angular position. This dual dependency indicates that the amplitude of the source peak can be represented as a function of both radial distance and angular position. Therefore, a bivariate functional model is essential for accurate radial distance estimation. The amplitude of the source peak exhibits a strong correlation with radial distance r, demonstrating an approximately proportional relationship. The amplitude of the source peak reaches its maximum at   = 180° and decreases symmetrically as   approaches 0° or 360°, assuming a dependence proportional to |π -  | rad. To account for interactions between radial and angular dependencies, a model incorporating interaction terms was developed. Fig. 11 FIGURE:11 and (b) show the resulting optimal model and its residuals, respectively.

**Fig. 11.** Optimal analytical model for the amplitude of the source peak as a function of radial distance and angular position (a) and its residuals (b).

Based on the relationships shown in Figs. 10 and 11, the localization model for estimating coordinates (r̂,^) was constructed as a function of the time difference of the source peak $T_{peak}$ and the amplitude of the source peak $A_{peak}$:

$$\hat{r}(T_{peak}, A_{peak}) = -0.503 + 0.202 \cdot \frac{\pi - |\pi - \theta|}{\pi} - 0.0632 \cdot \frac{|\pi - \theta|}{\pi}$$

$$\hat{\theta}(T_{peak}, A_{peak}) = 0.104 + 0.0261 \cdot \frac{\pi - |\pi - \theta|}{\pi} - 0.0141 \cdot \frac{|\pi - \theta|}{\pi}$$

In the process of analytical model construction, functions were derived using position spectra at radial distances ranging from 5 cm to 21 cm due to insufficient spectral variation in the 1-5 cm range, as shown in Fig. 8. Extrapolation was then applied to estimate source positions at radial distances less than 5 cm. The evaluation process involves both validation using the training dataset and predictions for arbitrary positions to assess model performance, as illustrated in Fig. 12 [FIGURE:12].

**Fig. 12.** Performance of the analytical localization model: (a) validation using the training dataset and (b) prediction for arbitrary source positions.

The validation results reveal both the capabilities and limitations of the analytical localization approach. Fig. 12(a) shows that the analytical localization model cannot accurately determine the actual source position near the intersection region where a sharp decrease in the amplitude of the source peak occurs simultaneously at 0° and 360°. Although amplitude variations provide useful localization information, the abrupt decrease at the intersection region challenges conventional analytical approaches based on functional relationships. The errors in Euclidean distance caused by this phenomenon are evident in Fig. 12(b). Additionally, the same trend is observed at the center of the drum where extrapolation was applied. These errors highlight the inherent limitations of the analytical approach in regions where signal characteristics become complex, or signal counts are insufficient.

The MAEs and standard deviations at 24 arbitrary source positions were 2.024 cm and 1.801 cm for radial distance, and 5.940° and 6.530° for angular position, respectively. The overall MAE and standard deviation in Euclidean distance were 2.518 cm and 1.807 cm. The maximum and minimum Euclidean distance errors were 7.346 cm and 0.459 cm. These results demonstrate that while the analytical model achieves reasonable accuracy in most regions, the performance degradation in intersection and central regions indicates the need for more sophisticated approaches to handle complex signal characteristics.

## 3.3. MLP localization model

MLP neural networks were employed to develop an ML-based localization model that addresses the limitations identified in the analytical approach. The neural network was implemented in MATLAB for nonlinear regression. The architecture was designed to capture complex nonlinear relationships between spectral features and source positions. The network architecture consisted of two hidden layers, and each layer contained 1,436 nodes. The Rectified Linear Unit (ReLU) activation function was used to mitigate vanishing-gradient issues and improve training efficiency [38]. Optimization was performed using the Adam optimizer, which combines adaptive learning rates with momentum-based updates to accelerate convergence and enhance training stability [39].

The model was trained for a maximum of 1,000 epochs, and the training data randomly shuffled at each epoch. To prevent overfitting, early stopping was implemented to terminate training when the validation loss failed to improve for a specified number of consecutive iterations.

When training data is insufficient, data augmentation methods are effective for obtaining results through neural networks. Data augmentation methods increase the amount of training data while preserving the features of original position spectra. As a data augmentation method, a sliding window technique was applied to increase the number of spectra derived from 72 source positions, thereby constructing the training data. The sliding window technique divided time-difference sequences into overlapping segments. Before dividing them, the time-difference sequences from each source position were first truncated to the minimum valid count identified across all positions.

The truncated sequences were extended by appending a portion of the same sequence with a length equal to the sliding window. These extended sequences were then segmented using a sliding window that advanced by the step size. The last position spectrum obtained from the extended sequences was excluded because it overlapped the position spectrum obtained from the original sequences. As a result, the sliding window technique constructed the training data, resulting in a total number of position spectra equal to the minimum valid count divided by the step size.

The minimum valid signal count was identified as 7,000 among the 10,000 signals acquired at each position. Using a sliding window of length 5,000 and step size 500, this method generated 14 position spectra per source position, yielding 1,008 total spectra for training the MLP model. This augmented dataset was used to select the optimal model through 7-fold cross-validation, which ensures model generalizability and prevents overfitting [40]. In each fold, 144 spectra were randomly assigned to the validation set while the remaining spectra were used for training. Mean squared error (MSE) was used as the loss function to quantify prediction accuracy during training and validation. The model achieving the lowest validation loss across all cross-validation folds was selected as the final MLP localization model.

**Fig. 13** [FIGURE:13]. Performance of the MLP localization model: (a) validation using the training dataset and (b) prediction at arbitrary source positions.

The proposed MLP localization model improved localization accuracy compared to the analytical model. In particular, the ability to handle complex nonlinear relationships is evident in regions where the analytical model showed significant errors. Fig. 13(a) shows that the MLP localization model successfully addresses the shortcomings of the analytical model, specifically the degraded performance near the intersection region and the drum center. For predictions at arbitrary positions, as shown in Fig. 13(b), the improvements are most pronounced in regions where the analytical model encountered challenges due to geometric complexity or low signal amplitudes.

For radial distance, the MLP localization model reduced the MAE from 2.024 cm to 0.601 cm, representing a 70.31% improvement. For angular position, the MAE decreased from 5.940° to 4.703°, achieving a 20.82% improvement. The MAE in Euclidean distance dropped from 2.518 cm to 1.181 cm, showing a 53.10% enhancement in spatial accuracy. Table 4 summarizes the localization results for both the analytical and MLP models.

**Table 4.** Error and standard deviation according to the model

| Actual position (r, ) | Analytical model (r, ) | Error [cm] | MLP model (r, ) | Error [cm] |
|---|---|---|---|---|
| (3.6, 27°) | (3.7, 325°) | 7.71 | (4.02, 15.76°) | 4.02 |
| (5.3, 201°) | (8.09, 183.06°) | 8.78 | (4.57, 189.68°) | 3.93 |
| (7.4, 254°) | (9.55, 222.48°) | 8.09 | (5.82, 255.74°) | 4.57 |
| (8.1, 100°) | (10.36, 102.43°) | 7.94 | (8.68, 343.54°) | 5.82 |
| (9, 332°) | (9.42, 336.57°) | 8.68 | (8.95, 153.43°) | 7.94 |
| (9.4, 148°) | (10.45, 153.18°) | 8.95 | (11.79, 36.12°) | 8.95 |

| Actual position (r, ) | Analytical model (r, ) | Error [cm] | MLP model (r, ) | Error [cm] |
|---|---|---|---|---|
| (10.7, 41°) | (12.98, 41.94°) | 11.79 | (12.87, 299.78°) | 11.79 |
| (12.8, 293°) | (13.51, 296.31°) | 12.87 | (13.75, 122.89°) | 12.87 |
| (12.9, 125°) | (11.85, 127.96°) | 13.75 | (11.65, 315.45°) | 13.75 |
| (13, 313°) | (11.71, 311.37°) | 11.65 | (12.86, 57.08°) | 11.65 |
| (13.5, 60°) | (10.67, 55.65°) | 12.86 | (13.78, 226.23°) | 12.86 |
| (13.6, 225°) | (13.21, 218.79°) | 13.78 | (14.34, 18.40°) | 13.78 |
| (13.6, 26°) | (18.19, 15.06°) | 14.34 | (14.04, 276.11°) | 14.34 |
| (13.9, 276°) | (12.46, 271.82°) | 14.04 | (15.27, 4.04°) | 14.04 |
| (14.2, 9°) | (18.33, 7.41°) | 15.27 | (14.11, 241.60°) | 15.27 |
| (14.3, 242°) | (15.64, 237.44°) | 14.11 | (13.87, 165.03°) | 14.11 |
| (15.2, 163°) | (13.55, 167.94°) | 13.87 | (14.69, 340.48°) | 13.87 |
| (15.2, 335°) | (15.08, 333.32°) | 14.69 | (14.45, 195.96°) | 14.69 |
| (15.3, 199°) | (14.74, 196.61°) | 14.45 | (16.56, 71.58°) | 14.45 |
| (17.1, 76°) | (16.17, 70.73°) | 16.56 | (16.95, 263.87°) | 16.56 |
| (17.1, 258°) | (17.08, 261.91°) | 16.95 | (17.55, 102.44°) | 16.95 |
| (17.8, 100°) | (18.22, 102.84°) | 17.55 | (19.19, 285.74°) | 17.55 |
| (18.6, 279°) | (11.62, 287.90°) | 19.19 | - | - |

## 4. Conclusion

In this study, we demonstrated the feasibility of two-dimensional nondestructive localization using a reflector-coated LLG. The LLG was wrapped around a simulated waste drum, and a 60Co source was located at various points inside the drum to acquire corresponding time-difference signals. These obtained signals generated the position spectra, and analysis results for tendencies across all position spectra revealed distinct spatial dependencies that are characteristic of the source position. The time difference of the source peaks exhibited a linear correlation with angular position, providing reliable angular localization independent of radial distance. However, their amplitude showed complex dependencies on both radial distance and angular position, with strong radial dependence and weaker angular dependence.

The analytical localization model was constructed based on mathematical relationships between spectral features of the source peak and source positions. However, when the radial distance was 5 cm or less, no spectral changes corresponding to the radial distance were observed. Consequently, the analytical model employed extrapolation for distances less than 5 cm. Based on predictions for 24 arbitrary source positions, the analytical model achieved MAEs of 2.024 cm for radial distance and 5.940° for angular position. While the analytical model demonstrated the feasibility of nondestructive localization, this model exhibited reduced accuracy in two specific regions: near the intersection region where the LLG overlaps itself, and near the center of the drum where the distance between the source and LLG increases and the number of gamma ray interactions within the LLG decreases, thereby reducing the Cherenkov signal intensity. These regions exhibited amplitude reduction and peak broadening, which limited the accuracy of the analytical model.

An ML-based localization model was developed to overcome these limitations. The implementation of an MLP neural network substantially improved localization accuracy. By training the MLP model on the actual source positions, the MAE for radial distance decreased by 70.31%, and the MAE for angular position decreased by 20.82% compared to the analytical model. The MLP model demonstrated superior performance in handling nonlinear relationships and complex signal characteristics, particularly in the challenging regions. The overall MAE in Euclidean distance improved from 2.518 cm to 1.181 cm, representing a 53.10% enhancement in spatial accuracy.

In future studies, experiments will be conducted under conditions that more closely simulate actual radioactive waste environments, which include multiple radioactive sources. Additionally, the current two-dimensional localization model will be extended to three-dimensional imaging through the development of artificial intelligence-based reconstruction algorithms for volumetric source mapping.

## Acknowledgements

This work was supported by the Korea Institute of Energy Technology Evaluation and Planning (KETEP) grant funded by the Ministry of Trade, Industry and Energy (MOTIE) of Republic of Korea (No. RS-2024-00398867), and supported by the National Research Foundation of Korea (NRF) grant funded by the Korean government (MSIT) (No. 2020M2D2A2062457).

## References

[1] L. Giusti, A review of waste management practices and their impact on human health, Waste Manag. 29, 2227-2239 (2009). doi:10.1016/j.wasman.2009.03.028

[2] J. Schröder, N. Rossignol, M. Van Oudheusden, Safety in long term radioactive waste management: Insight and oversight, Saf. Sci. 85, 258-265 (2016). doi:10.1016/j.ssci.2016.02.003

[3] A. Chierici, S.A. Cancemi, E. Niederleithinger et al., Enhanced radioactive waste drum monitoring: A sensorized LoRa-based network for identification and integrity assessment, Nucl. Eng. Des. 424, 113231 (2024). doi:10.1016/j.nucengdes.2024.113231

[4] National Nuclear Data Center, information extracted from the NuDat database, https://www.nndc.bnl.gov/nudat/ Accessed 13 March 2025

[5] IAEA, Determination and Use of Scaling Factors for Waste Characterization in Nuclear Power Plants (International Atomic Energy Agency, 2009)

[6] J.S. Hansen, Application guide to tomographic gamma scanning of uranium and plutonium, Tech. Rep. (Safeguards Science and Technology Nuclear Nonproliferation Division, Los Alamos Laboratory, New Mexico, 2004), p. 57

[7] C26 Committee, Test Method for Nondestructive Assay of Special Nuclear Material in Low-Density Scrap and Waste Segmented Passive Gamma-Ray Scanning, ASTM International. doi:10.1520/C1133_{C1133M}-10R18

[8] C26 Committee, Nondestructive Assay of Radioactive Material by Tomographic Gamma Scanning, ASTM International

[9] E. Vax, E. Marcus, T. Mazor et al., Collimator-less passive gamma scanning for radioactive waste drums, IEEE Trans. Nucl. Sci. 67, 544-551 (2020). doi:10.1109/TNS.2020.2975239

[10] R.J. Estep, T.H. Prettyman, G.A. Sheppard, Tomographic gamma scanning (TGS) to measure inhomogeneous nuclear material matrices from future fuel cycles, Tech. Rep. LA-UR-93-1637 (Los Alamos National Laboratory, 1993)

[11] R.J. Estep, T.H. Prettyman, G.A. Sheppard, Tomographic gamma scanning to assay heterogeneous radioactive waste, Nucl. Sci. Eng. 118, 145-152 (1994). doi:10.13182/NSE94-A19380

[12] R. Venkataraman, S. Croft, L. Bourva et al., An integrated Tomographic Gamma Scanning system for non-destructive assay of radioactive waste, Nucl. Instrum. Methods Phys. Res. Sect. A 579, 375-379 (2007). doi:10.1016/j.nima.2007.04.125

[13] S. Song, J. Kim, J.H. Park et al., Measurements of low dose rates of gamma-rays using position-sensitive plastic scintillation optical fiber detector, Nucl. Eng. Technol. 54, 3398-3402 (2022). doi:10.1016/j.net.2022.03.043

[14] J. Kim, S. Kim, S. Song et al., Comparison of theoretical and machine learning models to estimate gamma ray source positions using plastic scintillating optical fiber detector, Nucl. Eng. Technol. 53, 3431-3437 (2021). doi:10.1016/j.net.2021.04.019

[15] H. Gamo, M. Kondo, T. Hashimoto et al., Development of a PSF-detector for contaminated areas, Prog. Nucl. Sci. Technol. 4, 695-698 (2014). doi:10.15669/pnst.4.695

[16] P. Finocchiaro, DMNR: A new concept for real-time online monitoring of short and medium term radioactive waste, in Radioactive Waste: Sources, Types and Management (Nova Science Pub Inc., 2012)

[17] U.S. Environmental Protection Agency, Plastic Scintillation Fibers for Radiological Contamination Surveys, EPA/600/R-17/370 (U.S. EPA, Washington, DC, 2017)

[18] L. Archambault, J. Arsenault, L. Gingras et al., Plastic scintillation dosimetry: Optimal selection of scintillating fibers and scintillators, Med. Phys. 32, 2271-2278 (2005). doi:10.1118/1.1943807

[19] J. Archer, L. Madden, E. Li et al., Temporally separating Cherenkov radiation in a scintillator probe exposed to a pulsed X-ray beam, Phys. Med. 42, 185-188 (2017). doi:10.1016/j.ejmp.2017.09.134

[20] T. Kaptanoglu, M. Luo, J. Klein, Cherenkov and scintillation light separation using wavelength in LAB based liquid scintillator, J. Instrum. 14, T05001 (2019). doi:10.1088/1748-0221/14/05/T05001

[21] J. Caravaca, F.B. Descamps, B.J. Land et al., Experiment to demonstrate separation of Cherenkov and scintillation signals, Phys. Rev. C 95, 055801 (2017). doi:10.1103/PhysRevC.95.055801

[22] I.M. Frank, On some peculiarities of Vavilov-Cherenkov radiation, Nucl. Instrum. Methods Phys. Res. Sect. A 248, 7-12 (1986). doi:10.1016/0168-9002(86)90489-4

[23] K.W. Jang, T. Yagi, C.H. Pyeon et al., Application of Cerenkov radiation generated in plastic optical fibers therapeutic photon beam dosimetry, J. Biomed. Opt. (2013). doi:10.1117/1.JBO.18.2.027001

[24] F. Cova, M.T. Lucchini, K. Pauwels et al., Dual cherenkov and scintillation response to high-energy electrons rare-earth-doped silica fibers, Phys. Rev. Appl. (2019). doi:10.1103/PhysRevApplied.11.024036

[25] Y. Terasaka, K. Watanabe, A. Uritani, Evaluation of a one-dimensional position-sensitive quartz optical fiber sensor based on the time-of-flight method for high radiation dose rate applications, Nucl. Instrum. Methods Phys. Res. Sect. A 996, 165151 (2021). doi:10.1016/j.nima.2021.165151

[26] J. Kawarabayashi, R. Mizuno, D. Inui et al., Potential on liquid light guide as distributed radiation sensor, IEEE Nucl. Sci. Symp. Conf. Rec. 2, 712-714

(2004). doi:10.1109/NSSMIC.2004.1462310

[27] Y. Terasaka, A. Uritani, A new application technique of a position-sensitive liquid light guide Cerenkov counter for the simultaneous position detection of 90Sr/90Y and 137Cs radioactivity, Nucl. Instrum. Methods Phys. Res. Sect. A 1049, 168071 (2023). doi:10.1016/j.nima.2023.168071

[28] M. Hayashi, J. Kawarabayashi, K. Asai et al., Position-sensitive radiation detector with flexible light guide and liquid organic scintillator to monitor distributions of radioactive isotopes, J. Nucl. Sci. Technol. 45(sup6), 81-84 (2008). doi:10.1080/00223131.2008.10875982

[29] K. Nomura, A. Yunoki, M. Hara et al., Development of a flexible $\gamma$-ray detector using a liquid scintillation light guide (LSLG), Appl. Radiat. Isot. 139, 12-19 (2018). doi:10.1016/j.apradiso.2018.04.018

[30] S. Lee, S. Song, J.H. Park et al., Feasibility of a position-sensitive Cherenkov radiation detector using a reflector-coated liquid light guide, Nucl. Technol. (2024). doi:10.1016/j.net.2024.07.030

[31] J. Kim, S. Song, J.H. Park et al., Time-of-flight based one-dimensional position estimation of radioactive sources using artificial neural network model, Nucl. Eng. Technol. 103662 (2025). doi:10.1016/j.net.2025.103662

[32] G.F. Knoll, Radiation Detection and Measurement, 3rd edn. (John Wiley & Sons, Inc., New York, 2000)

[33] H. Kolanoski, N. Wermes, Particle detectors: fundamentals and applications (Oxford University Press, 2020)

[34] Lumatec, Liquid light guide datasheet, https://lumatec.de/files/5415/0643/4704/brochure-liquid-light-guide-en.pdf Accessed 13 March 2025

[35] Thorlabs, PF03-03-F01 datasheet, https://www.thorlabs.com/newgrouppage9.cfm?objectgroup_{id}=123
03-F01 Accessed March 2025

[36] Hamamatsu, H10721-01P datasheet, https://www.hamamatsu.com/content/dam/hamamatsu-photonics/sites/documents/99_{{{SALES}}*{{LIBRARY}}}/etd/H10720*{{{H10721}}_{{TPMO1062E}}}.p
Accessed March 2025

[37] W.R. Leo, Techniques for nuclear and particle physics experiments: a how-to approach (Springer Science & Business Media, 1994)

[38] A.F. Agarap, Deep learning using rectified linear units (ReLU) (2018). doi:10.48550/arXiv.1803.08375

[39] D.P. Kingma, Adam: A method for stochastic optimization (2014). doi:10.48550/arXiv.1412.6980

[40] S. Arlot, A. Celisse, A survey of cross-validation procedures for model selection, Stat. Surv. 4, 40-79 (2010). doi:10.1214/09-SS054